Research Article

Journal of Environmental Nanotechnology

Synergistic TiO_2 Nanosheets and Nitrogen-doped Carbon-coated $NiCo_2O_4$ Nanocomposite for High-performance Hybrid Supercapacitors

M. Vadivel[1*], M. Haitham Hadidi[2], Rajasekaran Saminathan[2], S. Madhuri Bhagat[3] and P. Satishkumar[4]

[1]Department of Civil Engineering, Nehru Institute of Technology, Coimbatore, India
[2]Department of Mechanical Engineering, College of Engineering and Computer Science, Jazan University, Jazan, Kingdom of Saudi Arabia
[3]Department of Civil Engineering, Yeshwantrao Chavan College of Engineering, Nagpur, MH, India
[4]Department of Mechanical Engineering, Rathinam Technical Campus, Coimbatore, TN, India
Received: 23.12.2025 Accepted: 07.02.2026 Published: 30.03.2026
*vadivelnitcbe@gmail.com

ABSTRACT

With the growing demand for high-performance energy storage devices, the development of electrode materials with high conductivity, large surface area, and long cycling stability is crucial. Nickel cobaltite coated with nitrogen-doped carbon nanoparticles ($NiCo_2O_4$@N-C) and its TiO_2-integrated nanocomposite ($NiCo_2O_4$@N-C/TiO_2) were successfully synthesized using a combined chemical route and ultrasonication technique. The novelty of this work lies in the synergistic integration of carbon-coated $NiCo_2O_4$ with conductive TiO_2 nanosheets, which suppresses nanoparticle agglomeration and enhances charge-transfer pathways. The nanocomposite exhibited improved electrical conductivity (1.9×10^{-3} S/m) compared to its pristine counterpart due to the interconnected conductive network formed by the TiO_2 nanosheets and the nitrogen-doped carbon coating. The enlarged effective surface area and improved electrolyte accessibility resulted in a high gravimetric capacitance of 709 F/g at 1 A/g, with 80% capacitance retention after 10^3 charge–discharge cycles. Electrochemical impedance spectroscopy revealed a low charge-transfer resistance (~20 Ω), indicating accelerated redox kinetics and enhanced pseudocapacitive behavior. The dual role of TiO_2 nanosheets as both a capacitive contributor and a conductive matrix plays a key role in boosting electrochemical performance. These findings demonstrate that the $NiCo_2O_4$@N-C/TiO_2 nanocomposite is a promising electrode material for high-performance hybrid supercapacitor applications.

Keywords: Supercapacitors; Gravimetric capacitance; Nanocomposites; Electrochemical Impedance Spectroscopy; Nickel cobaltite.

1. INTRODUCTION

The rapid depletion of fossil fuels and the intermittency of renewable energy sources have intensified demand for efficient energy storage technologies that deliver high power density, fast charge–discharge rates, and long-term stability. At the same time, the miniaturization of portable and wearable electronic devices has accelerated research into compact electrochemical energy storage systems. In this context, supercapacitors have emerged as promising devices, bridging the gap between conventional capacitors and batteries by offering high power density, excellent cycling life, and reliable operation (Satishkumar *et al.* 2020).

Among various electrode materials, spinel-structured nickel cobaltite ($NiCo_2O_4$) has attracted considerable attention due to its multiple redox-active sites, superior electrical conductivity compared to single-metal oxides, and favorable electrochemical kinetics. The presence of dual anion-active sites in $NiCo_2O_4$ facilitates rapid ion diffusion and redox reactions, leading to high charge-storage capability and cycling stability (Kannangara *et al.* 2024; Jiang *et al.* 2025). However, pristine $NiCo_2O_4$ often suffers from particle agglomeration, limited active surface area, and insufficient long-term electrical stability, which restricts its practical supercapacitor performance.

To overcome these limitations, extensive efforts have been directed toward structural engineering and hybridization strategies. Integration of $NiCo_2O_4$ with conductive carbonaceous materials such as graphene, reduced graphene oxide, carbon nanotubes, and MXenes has been shown to improve electrical conductivity and enhance electron transport pathways. For example, $NiCo_2O_4$-based heterostructures with MXene (Zhang *et al.* 2025; Shen *et al.* 2023) and graphene frameworks (Wu *et al.* 2025; Zhu *et al.* 2024) demonstrate enhanced electrochemical activity due to improved interfacial charge transfer and accessible active sites. Similarly,

compositional modulation through heterojunction formation or elemental doping has been reported to regulate band structure and accelerate redox kinetics, thereby improving cycling durability (Kizhepat *et al*. 2025; Sasmal *et al*. 2024).

In parallel, compositional modulation via heterojunction construction, elemental doping, and core–shell architectures has been shown to regulate the band structure, increase active site density, and accelerate redox kinetics (Khawale *et al.* 2024; Ran *et al.* 2024; Sun and Jian, 2024). A $NiCo_2O_4$@NiFeMn-LDH core–shell electrode was fabricated on carbon cloth to enhance charge transport and active site accessibility. The electrode delivered 6700 mF cm^{-2} with excellent rate capability and cycling stability in flexible devices (Zhang *et al.* 2025). Carbon coating, especially nitrogen-doped carbon, has emerged as an effective strategy to enhance electrical conductivity, suppress agglomeration, and stabilize electrode materials during repeated charge–discharge cycling (Yuan *et al.* 2023; Ni *et al.* 2023). When combined with a suitable secondary oxide matrix, such coatings can further improve surface area utilization and electrochemical reversibility. However, a nanocomposite system integrating nitrogen-doped carbon–coated $NiCo_2O_4$ with TiO_2 nanosheets for supercapacitor applications has not yet been reported.

In this work, $NiCo_2O_4$ nanoparticles were synthesized and modified through nitrogen-doped carbon coating to enhance conductivity and structural stability. Furthermore, a $NiCo_2O_4$@N-C/TiO_2 nanocomposite was developed using a chemical synthesis route coupled with ultrasonication to achieve uniform dispersion and strong interfacial contact. The electrochemical performances of pristine $NiCo_2O_4$, $NiCo_2O_4$@N-C, and $NiCo_2O_4$@N-C/TiO_2 electrodes were systematically investigated and compared. The improved performance of the nanocomposite is attributed to synergistic interactions among $NiCo_2O_4$ nanoparticles, nitrogen-doped carbon coating, and TiO_2 nanosheets, which collectively enhance charge transport, redox kinetics, and cycling stability, making the proposed material a promising candidate for advanced hybrid supercapacitor applications.

2. MATERIALS AND METHODS

2.1 Chemicals Used

Nickel (II) nitrate hexahydrate ($Ni(NO_3)_2 \cdot 6H_2O$), cobalt (II) nitrate hexahydrate ($Co(NO_3)_2 \cdot 6H_2O$), and titanium (IV) isopropoxide [$Ti(OCH(CH_3)_2)_4$] were procured from Matrix Enterprises, Nagercoil, Tamil Nadu, India.

2.2 Synthesis of $NiCo_2O_4$@N-C Nanoparticles

$NiCo_2O_4$@N-C nanoparticles were synthesized via a single, metal–organic framework (MOF)-derived route, chosen for its ability to introduce uniform nitrogen-doped carbon coating. In a typical synthesis, $Ni(NO_3)_2 \cdot 6H_2O$ and $Co(NO_3)_2 \cdot 6H_2O$ were dissolved in N,N-dimethylformamide (DMF) with a molar ratio of 1:2, followed by the addition of 1,4-benzenedicarboxylic acid (BDC) as the organic linker. Triethylenediamine was introduced as a coordination modulator to regulate crystal growth. The homogeneous solution was transferred to a Teflon-lined autoclave and maintained at 100 °C for 24 h. The resulting Ni/Co-MOF precipitate was washed repeatedly with ethanol and dried under vacuum. The dried MOF precursor was carbonized at 450 °C for 2 h under a nitrogen atmosphere to generate nitrogen-doped carbon–coated Ni–Co composite. Subsequently, mild oxidation was performed at 230 °C in air for 2 h to convert the metallic phase into crystalline spinel $NiCo_2O_4$ while preserving the nitrogen-doped carbon shell, yielding $NiCo_2O_4$@N-C nanoparticles. The nitrogen content and bonding configuration in the carbon shell were later confirmed using X-ray photoelectron spectroscopy (XPS N 1s analysis).

2.3 Synthesis of Titanium Dioxide (TiO_2)

Titanium oxide (TiO_2) nanoparticles were produced using a wet chemical technique. 0.5 mol of titanium isopropoxide was introduced to 60 mL of acidic ethanol and agitated vigorously at ambient temperature. The mixture was subsequently transferred to an autoclave and heated at 190 °C for 2 h. Following the reaction, the solvent was evaporated to yield a white precipitate, which was then washed with distilled water until the pH was neutral. The product was dried at 80 °C and calcined at 430 °C for 4 h to get crystalline TiO_2 nanoparticles.

2.4 Synthesis of $NiCo_2O_4$@N-C/TiO_2 Nanocomposite

The $NiCo_2O_4$@N-C/TiO_2 nanocomposite was synthesized by the ultrasonication method. $NiCo_2O_4$@N-C nanoparticles (45 mg) were suspended in 166 mL of TiO_2 solution at a concentration of 30 mg/L. The resultant mixture was subjected to sonication for 2 h (Peng *et al*. 2020). Then the resultant black solution was subjected to drying at 110 °C for 24 h to provide the blackish $NiCo_2O_4$@N-C/TiO_2 nanocomposite.

2.5 Preparation of the Working Electrode

The working electrode was made by utilizing Nafion as a binder to affix the prepared samples and ethanol as a solvent onto carbon paper. Nafion binder was employed for its superior ionic permeability, while carbon paper was utilized for its enhanced stability during redox reactions. Due to its superior electronic conductivity, carbon paper reduces the equivalent series resistance during electrochemical measurements. Finely milled materials were combined with ethanol and Nafion

to establish a uniform suspension. The prepared suspension was uniformly coated onto a carbon paper electrode, followed by drying at 60 °C overnight. Dry mass loading of the deposited substance upon the carbon paper electrode was 1.3 mg.

2.6 Properties of the Materials

XRD analysis was conducted using a Bruker D8 Advance diffractometer (Germany). FTIR spectra of the materials were recorded from 4000 to 400 cm^{-1}. FESEM and EDX analyses of the prepared specimens were performed using a JEOL JCM-6000 Plus and a ZEISS Gemini scanning electron microscope to examine their surface morphology and elemental composition (Edlabadkar et al. 2025). Brunauer–Emmett–Teller analysis of the samples was conducted to determine the pore size and surface area. Current–voltage measurements were conducted using a Model 6487 Picoammeter/Voltage Source to evaluate the electrical conductivity of the prepared specimens. Thermogravimetric analysis was conducted using a TG8120 device from ambient temperature to 900 °C. UV–Visible absorption measurements were performed using a Cary 60 UV–Visible spectrometer to investigate the reduction-induced electronic structure modification of TiO_2. X-ray photoelectron spectroscopy (XPS) was employed to quantify nitrogen incorporation and analyze the chemical bonding states in the nitrogen-doped carbon coating of $NiCo_2O_4$@N-C. High-resolution N 1s spectra were deconvoluted into pyridinic-N (~398.3 eV), pyrrolic-N (~400.1 eV), and graphitic-N (~401.2 eV) components, confirming successful nitrogen doping. The relative contributions of graphitic and pyridinic nitrogen indicate enhanced electronic conductivity and increased electrochemically active sites, which are beneficial for charge-transfer kinetics.

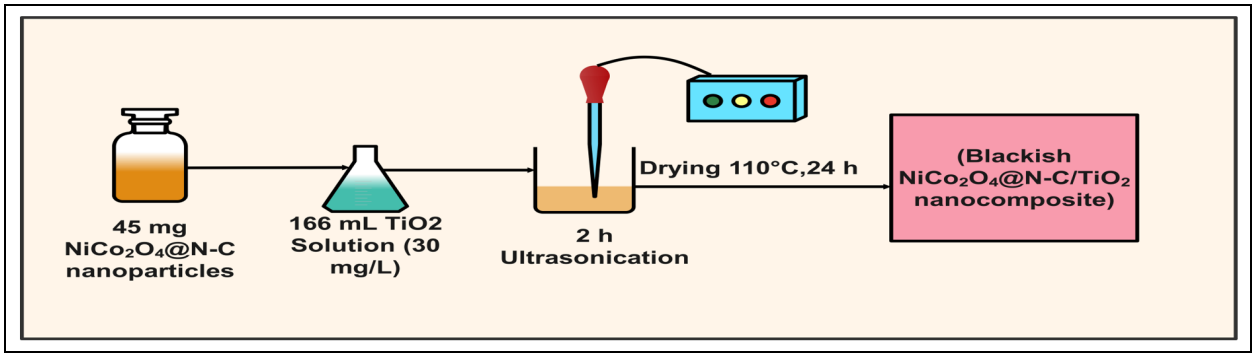


Fig. 1: Schematic illustration of $NiCo_2O_4$@N-C/TiO_2 nanocomposite fabrication

2.7 Electrochemical Characterizations

Electrochemical impedance spectroscopy (EIS), cyclic charge/discharge (CCD), and cyclic voltammetry (CV) tests were performed using Gamry Interface 5000 (06531). Electrochemical evaluations were conducted using a three-electrode setup in 4 M KOH electrolyte. The produced specimens were affixed to carbon paper to create a functioning electrode. Pt and silver/silver chloride electrodes served as the auxiliary and reference electrodes, respectively, throughout all electrochemical tests. CCD profiles and CV were acquired in a possible value of 0 V to 0.58 V. Discharge/cyclic charge examination was performed at varying present concentrations (1–5 A/g). EIS measurements were conducted using a sinusoidal wave with an amplitude of 5 mV and frequency 100 kHz to 0.1 Hz.

3. RESULTS AND DISCUSSION

3.1 TGA Evaluation

Fig. 2 depicts a thermogram of $Co(OH)_3$ recorded over a temperature spectrum from ambient temperature to 800 °C. Two distinct regions of weight loss are observed in the thermogram. The initial region of weight loss spans from 30 to 250 °C, during which approximately 8.87% mass loss is observed as a result of the elimination of intercalated or physically adsorbed water molecules. The second weight loss interval was between 288 and 349 °C, during which approximately 23.07% mass reduction transpires as a result of precursor dehydration to provide $NiCo_2O_4$. The absence of additional weight loss beyond 400 °C signifies total dehydration of $Co(OH)_3$ into $NiCo_2O_4$ nanoparticles.

3.2 X-ray Diffraction

XRD analysis of $NiCo_2O_4$NPs, $NiCo_2O_4$@N-C NPs, and $NiCo_2O_4$@N-C/TiO_2 nanocomposite was performed to investigate their crystal structures and phase compositions. As indicated in Fig. 3, XRD of $NiCo_2O_4$ shows a series of peaks positioned on 2θ of 22.8°, 34.3°, 39.3°, 46.4°, 54.4°, 60.2°, and 65.5°, which indexed to (111), (220), (311), (400), (422), (511), and (440) crystal planes. Diffraction peaks show slight shifts under minor deformation and 2θ readings; nevertheless, no significant peak expansion was observed, indicating

successful phase integration and maintaining the overall crystalline coherence of the composite material.

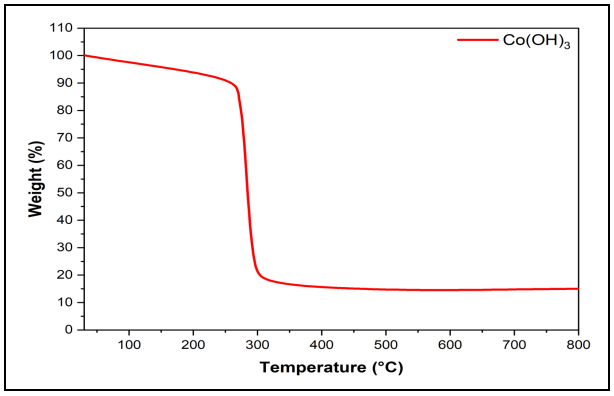


Fig. 2: Thermogravimetric analysis (TGA) of precursor $Co(OH)_3$ for temperatures up to 800 °C

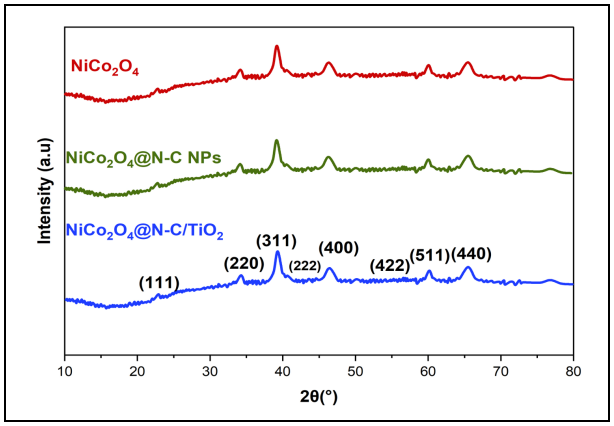


Fig. 3: XRD patterns of the pristine $NiCo_2O_4$NPs, $NiCo_2O_4$@N-C NPs, and $NiCo_2O_4$@N-C/TiO_2 nanocomposite

The mean crystallite size (D) of the $NiCo_2O_4$ nanoparticles was determined using the diffraction angle (θ) and the wavelength (λ) of X-ray:

$$D = \frac{0.9\lambda}{\beta \cos\theta} \quad \ldots (1)$$

The determined crystallite size of the pure nanoparticles ranged from 5 to 20 nm.

The diffraction peaks indicate superior crystallinity of the pure nanoparticles. The crystallinity of the nanoparticles was determined by using:

$$\text{Crystallinity (\%)} = \frac{\text{Area under the crystalline peaks}}{\text{Area of the all peaks}} \times 100 \ldots (2)$$

The determined percentage of crystallinity for pure nanoparticles were 72.3%.

X-ray density of unaltered $NiCo_2O_4$ nanoparticles was computed using:

$$\rho_x = \frac{8M}{N_A V} \quad \ldots (3)$$

In this context, 'V' represents the volume of the unit cell, whereas 'M' denotes the molecular weight and N_A denotes Avogadro's constant. Computed X-ray density was 5.7 g/cm³.

Pellets (0.2 g) of unaltered $NiCo_2O_4$ nanoparticles were prepared to determine the bulk density using:

$$\rho_b = \frac{m}{V} \quad \ldots (4)$$

The bulk density was found to be 4.83 g/cm³.

The percentage porosity of the synthesized nanoparticles was estimated using the data of bulk density and X-ray density:

$$\text{Porosity (\%)} = \left[1 - \frac{\rho_b}{\rho_x}\right] \times 100 \quad \ldots (5)$$

The calculated results indicate that the nanoparticles exhibit a porosity of 23.4%.

Error analysis was performed for crystallite size and porosity, and the results were reported as mean values with standard deviations to reflect experimental uncertainty. The average crystallite size of $NiCo_2O_4$ nanoparticles was calculated as 12.6 ± 2.1 nm, obtained from multiple diffraction peaks using the Scherrer equation, where the uncertainty arises from instrumental broadening and peak fitting. Similarly, the porosity was determined to be 23.4 ± 1.8%, with the deviation estimated from repeated bulk and X-ray density measurements, confirming good reproducibility of the structural parameters.

3.3 Fourier Transform Infrared Spectroscopy

An FTIR analysis was carried out on the synthesized $NiCo_2O_4$ powders to examine structural features and confirm phase formation after annealing. The spectra (Fig. 4) display two prominent absorption bands at approximately 502 cm^{-1} and 583 cm^{-1}, which are attributed to the stretching vibrations of Ni–O (octahedral sites) and Co–O (tetrahedral sites), respectively, confirming the formation of spinel $NiCo_2O_4$. The weak bands observed in the range of 1500–1600 cm^{-1} and the broad band around 3409 cm^{-1} are associated with H–O–H bending and O–H stretching vibrations of physically adsorbed moisture on the sample surface. The band near 1360 cm^{-1}, previously attributed to nitrate species, is reassigned to surface carbonate groups arising from atmospheric CO_2 adsorption after calcination. The absorption band around 1012 cm^{-1} is assigned to C–O/C–N stretching vibrations related to residual or carbonaceous species, while the weak band near 2892 cm^{-1} corresponds to C–H stretching vibrations of surface-adsorbed carbon species. Overall, the FTIR results

confirm the successful synthesis of spinel $NiCo_2O_4$ without the presence of undesired precursor residues.

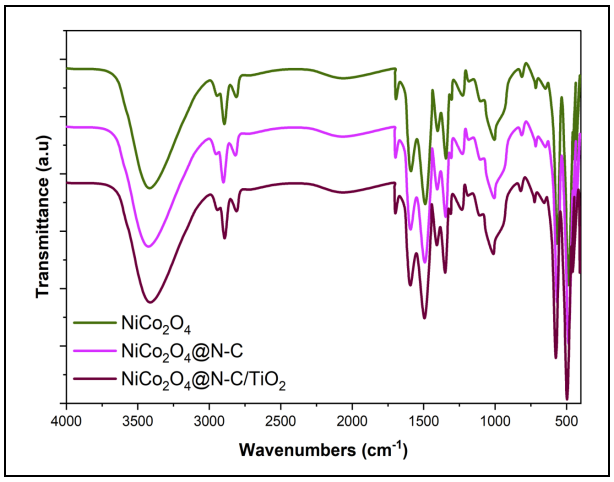


Fig. 4: FTIR spectra of the specimens

3.4 FESEM

Fig. 5 shows the FESEM images of $NiCo_2O_4$, $NiCo_2O_4$@N-C, and $NiCo_2O_4$@N-C/TiO_2 nanocomposites. The individual nanoparticles of $NiCo_2O_4$ amalgamated to form bigger, irregularly formed clusters. Dimensions of individual nanoparticles and aggregates ranged from 50 to 80 nm. Nanoparticles underwent sonication treatment before carbon covering. Sonication process effectively disrupted particle agglomerates and facilitated the homogeneous dispersion of nanoparticles (Selvaraju e*t al*. 2022). Post carbon-coating, the carbonaceous layer surrounding the nanoparticles protects them from agglomeration. Carbon-coated nanoparticles appear smaller than the unaltered $NiCo_2O_4$ aggregates. The C@Co_3CO_4 nanoparticles are intertwined with the titanium sheets.

3.5 EDX Analysis

Chemical purity of specimens was assessed by power dispersive X-ray spectroscopy examination. EDX spectrum of clean $NiCo_2O_4$ (Fig. 6a) reveals the presence of Ni, Co, and O elements. The atomic ratio of these elements is consistent with the stoichiometric composition of $NiCo_2O_4$. EDX spectrum of $NiCo_2O_4$@N-C (Fig. 6b) includes carbon atoms alongside cobalt and oxygen atoms. The EDX spectrum (Fig. 6c) confirms the presence of Ni, Co, Ti, and O elements, indicating the successful formation of the $NiCo_2O_4$@N-C/TiO_2 nanocomposite.

3.6 Brunauer–Emmett–Teller Analysis (BET)

Pore diameter of the synthesized specimens, particle size, and specific area were assessed using the BET analysis. Fig. 7 presents the N_2 adsorption–desorption isotherms of pristine $NiCo_2O_4$ nanoparticles, $NiCo_2O_4$@N-C nanoparticles, and the $NiCo_2O_4$@N-C/TiO_2 nanocomposite, with BET surface areas of 118 m^2/g, 23 m^2/g, and 54 m^2/g, respectively. All samples exhibit type-IV isotherms with hysteresis loops, indicating mesoporous structures. The corresponding pore size distribution curves for each sample are shown in the inset of the respective isotherms. The relatively lower surface area observed for the $NiCo_2O_4$@N-C sample (23 m^2/g) may be attributed to pore blockage and particle agglomeration caused by excessive carbon coating, which reduces the accessible surface area. In contrast, the incorporation of TiO_2 partially restores the porous structure, leading to an increase in surface area. The sharp rise in nitrogen adsorption at higher relative pressure ($P/P_0 > 0.8$) is associated with capillary condensation within mesopores.

The substantial pore diameter and surface area of the $NiCo_2O_4$@N-C and $NiCo_2O_4$@N-C/TiO_2 nanocomposite resulted from the mitigated aggregation resulting from carbon covering and incorporation of TiO_2, in that order. Substantial porous width of the $NiCo_2O_4$@N-C/TiO_2 nanocomposite primarily provides reduced diffusion resistance for electrolyte ions. Earlier studies have shown that the BET analysis confirms that the $NiCo_2O_4$@TiO_2 electrode possesses a higher specific surface area and porous architecture than pristine $NiCo_2O_4$, which enhances electrolyte diffusion, active site availability, and overall electrochemical performance (Xue *et al*. 2019).

The BET analysis reveals an apparent variation in surface area after carbon coating and subsequent TiO_2 incorporation. The decrease in surface area observed for $NiCo_2O_4$@N-C compared to pristine $NiCo_2O_4$ is attributed to partial pore blocking and surface encapsulation by the carbon coating, which reduces nitrogen accessibility during adsorption measurements. However, upon incorporation of TiO_2, the BET surface area increases for the $NiCo_2O_4$@N-C/TiO_2 nanocomposite due to suppressed nanoparticle agglomeration and the introduction of a porous TiO_2 matrix that restores accessible surface sites. This hierarchical structure facilitates improved electrolyte diffusion and ion transport, explaining the enhanced electrochemical performance despite the initial surface area reduction after carbon coating.

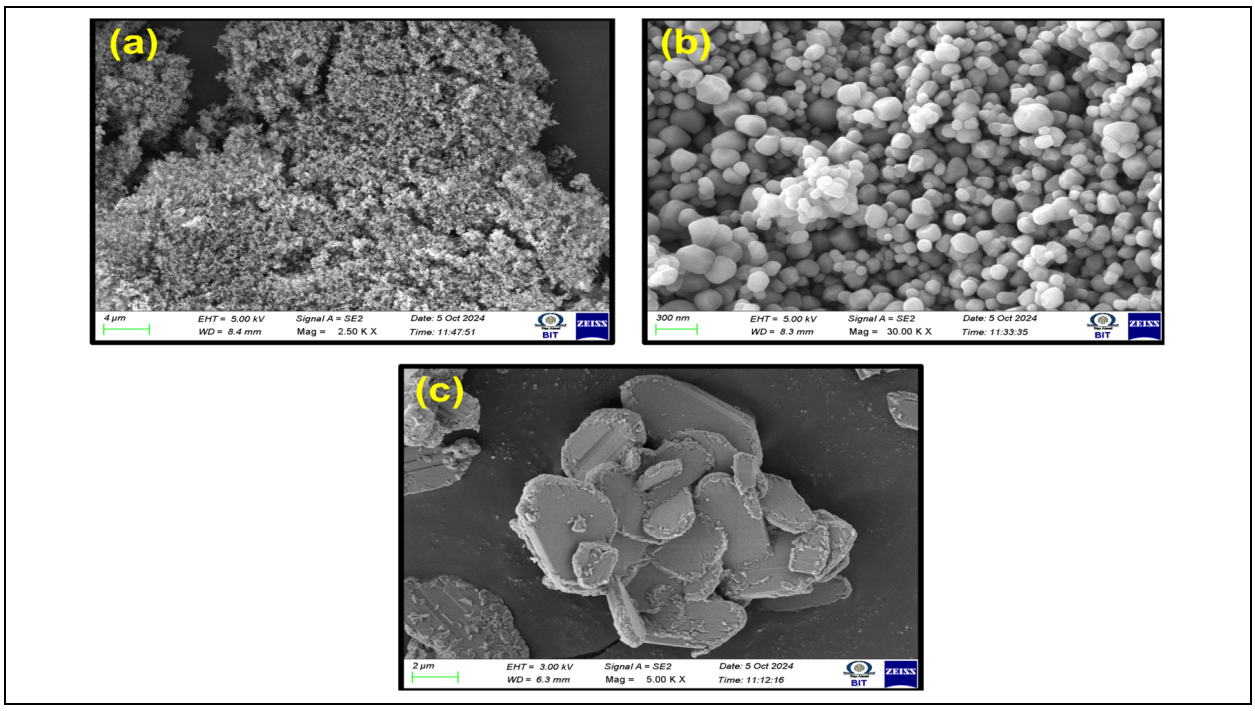
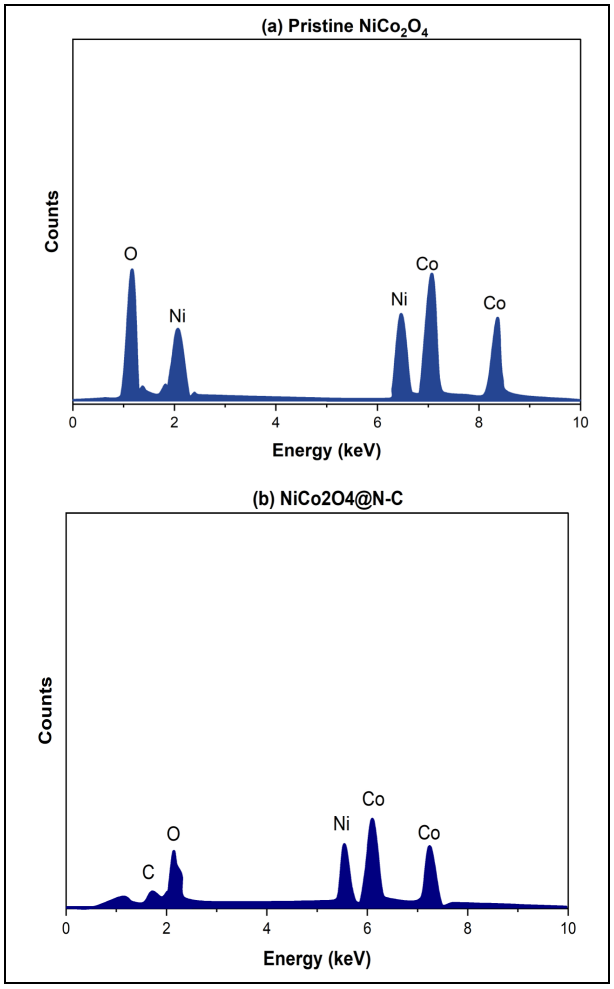


Fig. 5: FESEM images of: (a) $NiCo_2O_4$, (b) $NiCo_2O_4$@N-C and (c) $NiCo_2O_4$@N-C/TiO_2



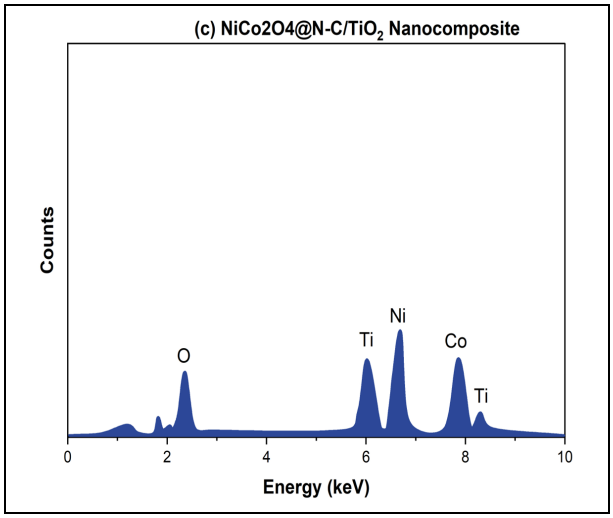


Fig. 6: EDX analyses of: (a) $NiCo_2O_4$, (b) $NiCo_2O_4$@N-C and (c) $NiCo_2O_4$@N-C/TiO_2

3.7 Thermogravimetric Analysis (TGA)

Fig. 8 illustrates the comparative TGA of clean $NiCo_2O_4$ and $NiCo_2O_4$@N-C nanoparticles, and the $NiCo_2O_4$@N-C/TiO_2 nanocomposite (Syed *et al*. 2024). The thermogram of the $NiCo_2O_4$@N-C/TiO_2 nanocomposite indicates a total weight loss of 88%, attributed to the burning of the coating and the desorption of adsorbed water and titanium carbon. Additional weight loss seen in the $NiCo_2O_4$@N-C/TiO_2 nanocomposite can be attributed to the combustion of TiO_2. Furthermore, the recorded weight reduction

(10.0%) closely approximates the percentage composition (12%) of TiO_2 within the nanocomposite.

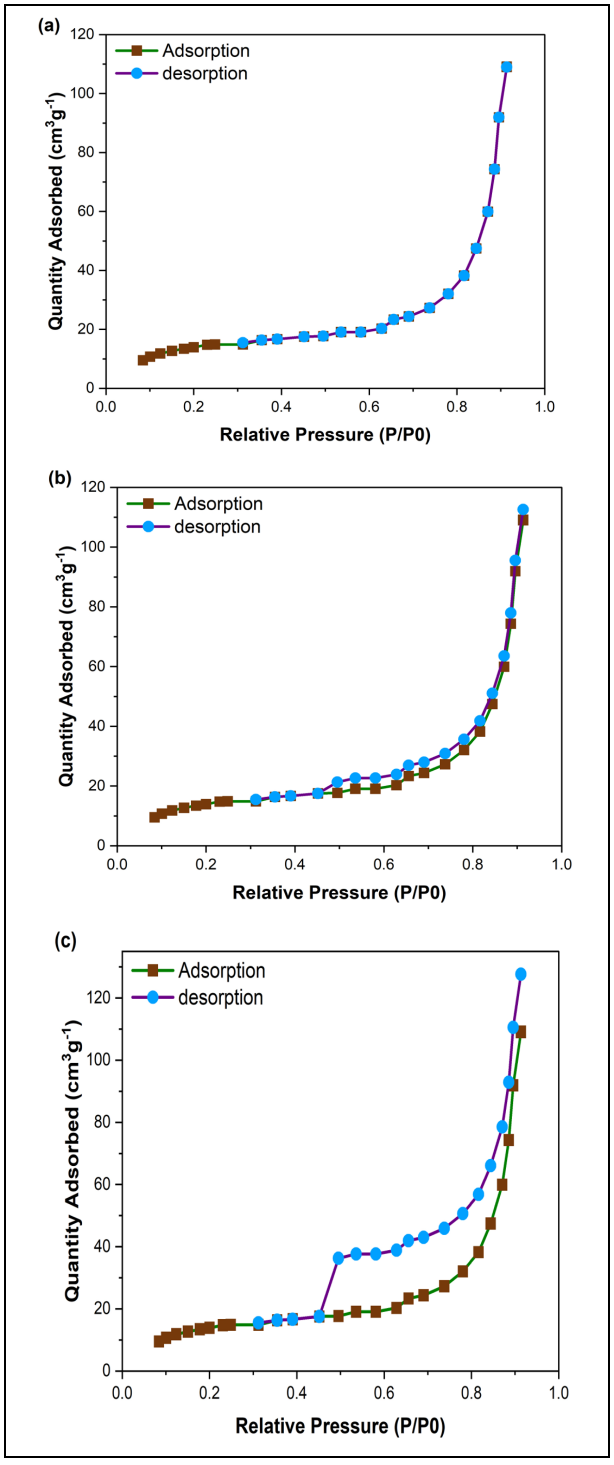


Fig. 7: Nitrogen adsorption–desorption isotherms of: (a) $NiCo_2O_4$, (b) $NiCo_2O_4$@N-C and (c) $NiCo_2O_4$@N-C/TiO_2

3.8 UV–Visible Spectroscopy

The optical characteristics of the nanoparticles were examined with a Systronics UV–Vis spectrometer. Fig. 9 illustrates the absorbance of TiO_2 in the nanoscale region at ambient temperature. The spectrum recorded in the wavelength range of 200–1200 nm was analyzed. A peak has been observed at 330.9 nm.

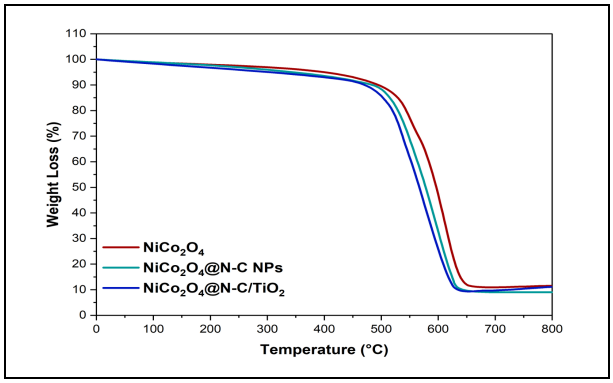


Fig. 8: TGA of the specimens

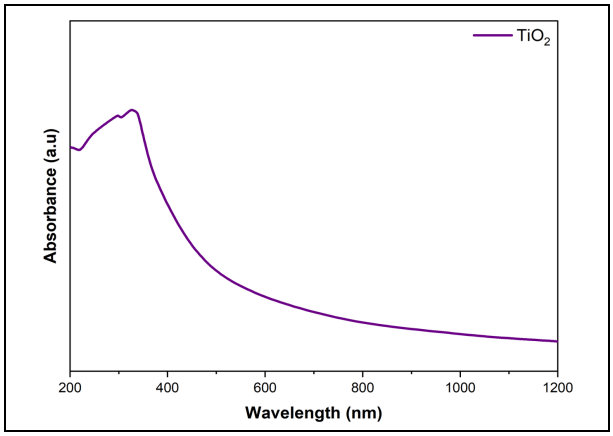


Fig. 9: UV–Vis spectroscopy of TiO_2

3.9 Evaluation of Current–voltage Characteristics

Current–voltage (I–V) measurements were conducted at ambient temperature over the voltage range of −5 V to +5 V. Fig. 10 illustrates the I–V characteristics of the pure $NiCo_2O_4$ and $NiCo_2O_4$@N-C nanoparticles, and the $NiCo_2O_4$@N-C/TiO_2 nanocomposite. Non-ohmic characteristics of the $NiCo_2O_4$ nanoparticles are apparent from their non-linear current-voltage curve. The almost straight curve of the $NiCo_2O_4$@N-C nanoparticles and the $NiCo_2O_4$@N-C/TiO_2 nanocomposite signifies enhanced electrical conductivity, resulting from the TiO_2 matrix and the highly conductive carbon paste. Electrical conductivity examinations were conducted by fabricating pellets from the assembled materials. Prior research has shown that $NaBH_4$-reduced $NiCo_2O_4$ nanosheets exhibit significantly improved electrical conductivity (1.9 S m^{-1}) due to the introduction of low-valence and oxygen-defect metal species, which in turn enables excellent rate capability with a 91.5% capacitance retention at 20 A g^{-1} and high specific capacitance of 1812 F g^{-1} (You *et al.* 2023).

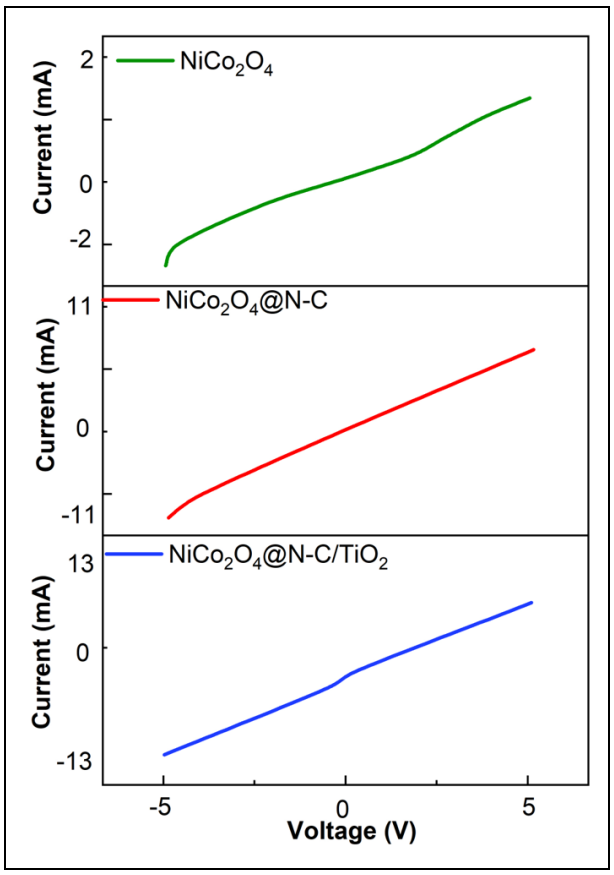


Fig. 10: I–V characteristics of the specimens

The electrical conductivity of the specimens (σ in S/m) was calculated by substituting the measured values of cross-sectional area (A) and thickness (l) of the pellets in:

$$\sigma = \frac{l}{RA} \quad \ldots (6)$$

The value of resistance, R, was determined by calculating the reciprocal of the slope of the acquired current-voltage pattern. $NiCo_2O_4$@N-C/TiO_2 nanocomposite demonstrated superior electrical conductivity compared to pure $NiCo_2O_4$@N-C (4.55 × 10−5 S/m) and $NiCo_2O_4$ nanoparticles (1.9 × 10−8 S/m).

Although the absolute electrical conductivity values of the synthesized materials fall in the range of 10^{-5}–10^{-8} S m^{-1}, such values are typical for pressed oxide-based electrode pellets and do not directly represent *in situ* electrode conductivity during electrochemical operation. In supercapacitor electrodes, overall performance is primarily governed by interfacial charge-transfer resistance, ionic transport through the electrolyte, and electron percolation pathways within the active material rather than bulk conductivity alone. The relative increase in conductivity observed for the $NiCo_2O_4$@N-C/TiO_2 nanocomposite, compared to pristine $NiCo_2O_4$ and $NiCo_2O_4$@N-C, confirms the formation of an improved conductive network facilitated by nitrogen-doped carbon coating and the TiO_2 matrix. This enhancement correlates well with the reduced charge-transfer resistance observed in EIS measurements and the superior electrochemical performance of the nanocomposite electrode.

3.10 Electrochemical Measurements

Electrochemical properties of the specimens were assessed by cyclic voltammetry (CV) studies of 4 M sodium hydroxide. CV identities of the three specimens were recorded at different sweep values throughout the potential range of 0 to 0.59 V.

CV repetitions of the pristine $NiCo_2O_4$ nanoparticles (Fig. 11a) exhibit irregularities that signify a redox process. The existence of redox peaks indicates nanoparticles primarily engage in a faradaic reaction for charge storage. Reduced region of the CV repetitions signifies the inadequate energy storage capacity of the $NiCo_2O_4$ electrodes. The marginally increased area of the CV loop for the $NiCo_2O_4$@N-C electrode (Fig. 11b) indicates enhanced pseudocapacitive behavior and improved electrical conductivity. Markedly greater region of the cyclic voltammetry iterations for the $NiCo_2O_4$@N-C/TiO_2 (Fig. 11c) compared to the cyclic voltammetry loops of the other two specimens resulted from the incorporation of TiO_2. The direct correlation and symmetrical cyclic voltammetry loops between the scan rate and intensity of redox peaks demonstrate enhanced reversible behavior of the nanocomposite electrode. CV demonstrates enhanced pseudocapacitive behavior of the $NiCo_2O_4$/activated carbon electrode with higher current response than pristine $NiCo_2O_4$ nanoflakes, using sol–gel synthesized $NiCo_2O_4$ and coconut shell–derived activated carbon as electrode materials (Bosco Franklin *et al*. 2024).

The inclusion of TiO_2 enhances the overall capacitance, reduces the internal resistance, and increases the surface area of the nanocomposite. The improved Faradaic response is attributed to enhanced electrode–electrolyte interfacial contact.

$$Co_3O_4 + OH^- + H_2O \rightarrow 3CoOOH + e^-$$

$$CoOOH + OH^- \rightarrow CoO_2 + H_2O + e^-$$

The consistent redox potential, regardless of varying clean values, indicates exceptional reversibility of the $NiCo_2O_4$@N-C/TiO_2 nanocomposite. Gravimetric capacitance of manufactured electrodes was determined using:

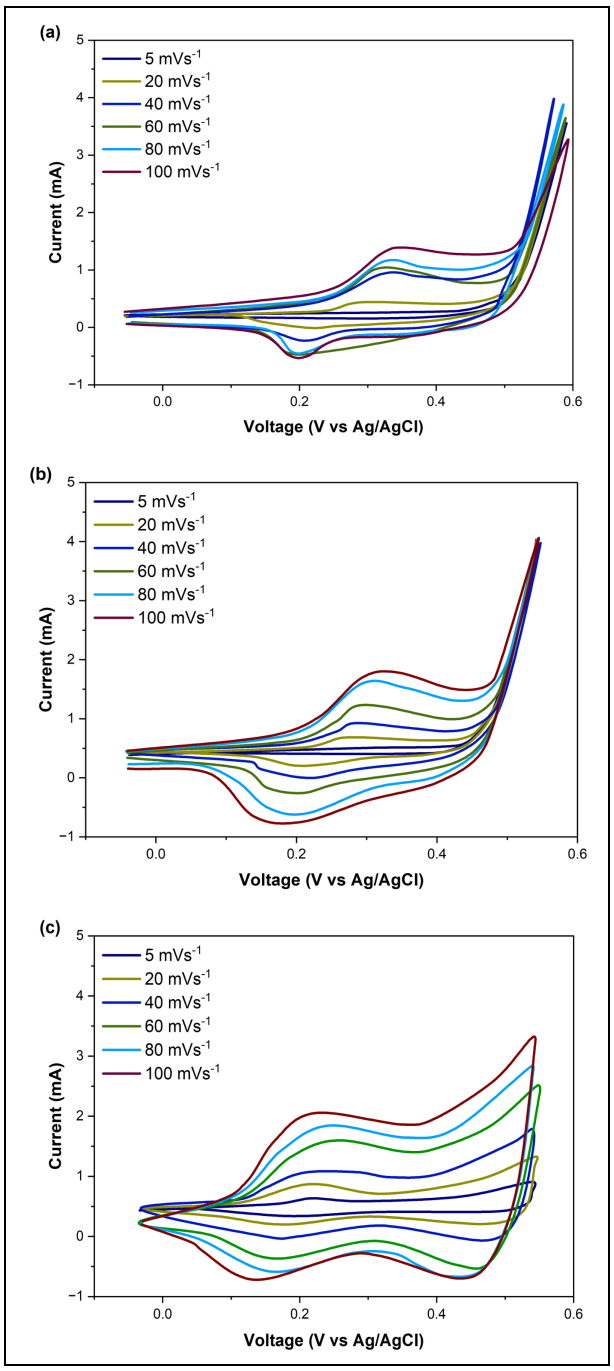


Fig. 11: CV profiles of $NiCo_2O_4$ and $NiCo_2O_4$-based electrodes

$$Q = \frac{\text{Integrated area } (\int IdV)}{\text{Scan rate } (v)} \quad \ldots (7)$$

$$C = \frac{\int Idv}{v \times \Delta V} \quad \ldots (8)$$

$$Csp = \frac{\int IdV}{v \times \Delta V \times m} \quad \ldots (9)$$

Superior gravimetric capacitance of $NiCo_2O_4$@N-C/TiO_2 nanocomposite compared to the pure $NiCo_2O_4$ NPs and $NiCo_2O_4$@N-C NPs at an identical scan rate results from the synergistic interaction between electric double-layer capacitance and faradic capacitance.

Fig. 12 illustrates the impact of scan rate on gravimetric capacitance. Electronically conductive carbon covering enhances and diminishes electrolyte resistance and electron transport. This resulted from the temporally constrained and surface-restricted involvement between the electrolyte and the analyte. At a reduced scan value, electrolyte ions have sufficient time to diffuse deeply into the electrode, hence maximizing surface area.

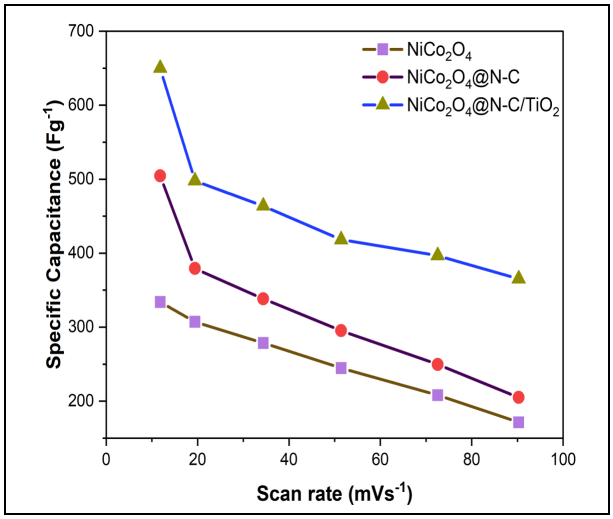


Fig. 12: Specific capacitance variation with sweep rate

Cyclic stability of produced specimens was evaluated over 10^3 cyclic voltammetry cycles at a sweep rate of 60 mV/s. The significant decrease in the region beneath cyclic voltammetry repetition after 1000 loops signifies inadequate cyclic reversibility of pure nanoparticles. CV curves of $NiCo_2O_4$@N-C nanoparticles demonstrate enhanced cyclic behaviour compared to pure $NiCo_2O_4$ nanoparticles, attributable to the carbon coating. The conductive carbon coating enhances electron transport and diminishes electrolyte resistance in electronic applications. Enhanced cyclic reversibility was noted in $NiCo_2O_4$@N-C/TiO_2 nanocomposite.

Correlation between the CV cycles and capacitance retention percentage was additionally assessed. Fig. 13 clearly reveals that the $NiCo_2O_4$@N-C/TiO_2 nanocomposite had a 29% loss, $NiCo_2O_4$@N-C/TiO_2 incurred a 29.50% loss, and pure $NiCo_2O_4$ nanoparticles suffered a 77.92% reduction in their original capacitance after 10^3 cyclic voltammetry cycles.

Fig. 14 illustrates the galvanostatic charge–discharge (GCD) curves of pure $NiCo_2O_4$ nanoparticles, $NiCo_2O_4$@N-C nanoparticles, and the $NiCo_2O_4$@N-CNPs/TiO_2 nanocomposite electrodes at a current density of 1 A/g. The triangular CCD profile and extensive

elongation of $NiCo_2O_4$@N-C/TiO_2 nanocomposite demonstrate its enhanced electrochemical activity compared to the pristine $NiCo_2O_4$ and $NiCo_2O_4$@N-C nanoparticles.

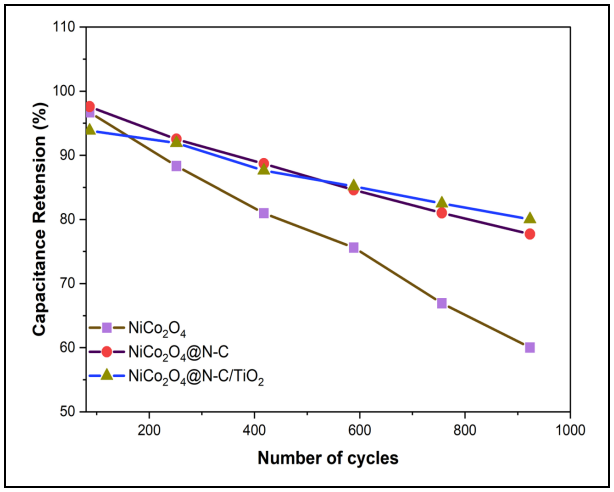


Fig. 13: Capacitance retention vs. CV cycles

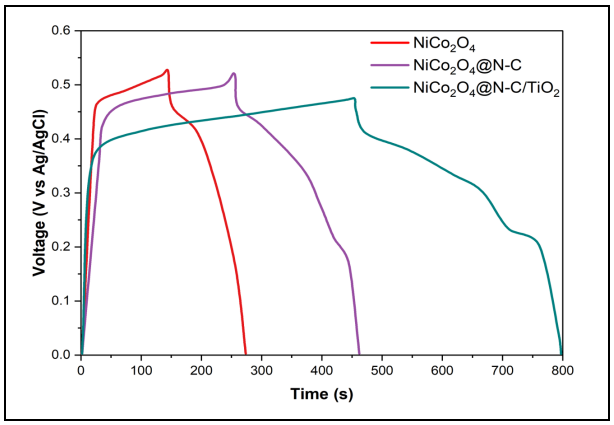


Fig. 14: GCD profiles of $NiCo_2O_4$ and hybrid electrodes at 1 A g^{-1}

Gravimetric capacitance (C_g) of the synthesized electrodes was determined by substituting relevant voltage drop (ΔV), discharge duration (Δt), and values of current density during release in:

$$C_g = \frac{i \times \Delta t}{\Delta V} \quad \ldots (10)$$

C_g of the nanocomposite at a density of 1 A/g was 709 F/g. The nanocomposite demonstrates a significantly greater C_g compared to the pristine $NiCo_2O_4$@N-C NPs (321 F/g) and $NiCo_2O_4$ NPs (502 F/g). Previous studies demonstrated that the amorphous carbon–modified $NiCo_2O_4$ was deposited on nickel foam (C/$NiCo_2O_4$/NF) to serve as the electrode material. GCD results showed high capacitance 379.4 mF cm^{-2} at 1.5 mA cm^{-2} with 87.1% capacitance retention (Yang *et al*. 2024). The influence of current density on the gravimetric capacitance of the electrodes was examined, and the results are depicted in Fig. 15.

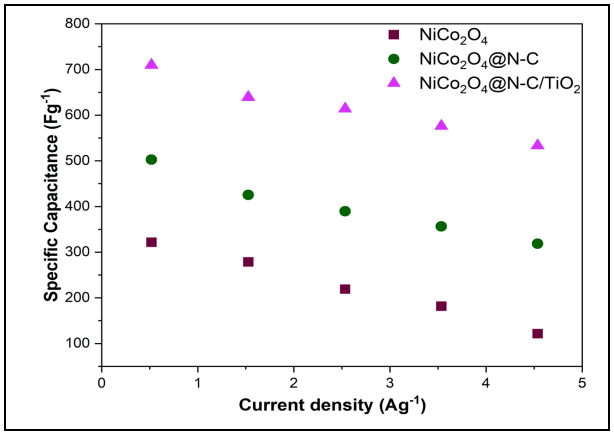


Fig. 15: Variation of gravimetric capacitance with current density for the specimens

Fig. 16 shows the Nyquist plots and fitted impedance spectra of the $NiCo_2O_4$-based electrodes. The intercept at the high-frequency end on the Z′ axis corresponds to the solution resistance (R_s). The semicircular arc in the high-to-middle frequency region is attributed to the charge-transfer resistance (R_{ct}) at the electrode/electrolyte interface. The inclined line in the low-frequency region is associated with Warburg diffusion impedance, indicating ion transport within the electrode and electrolyte. A steeper low-frequency line generally suggests improved capacitive behavior

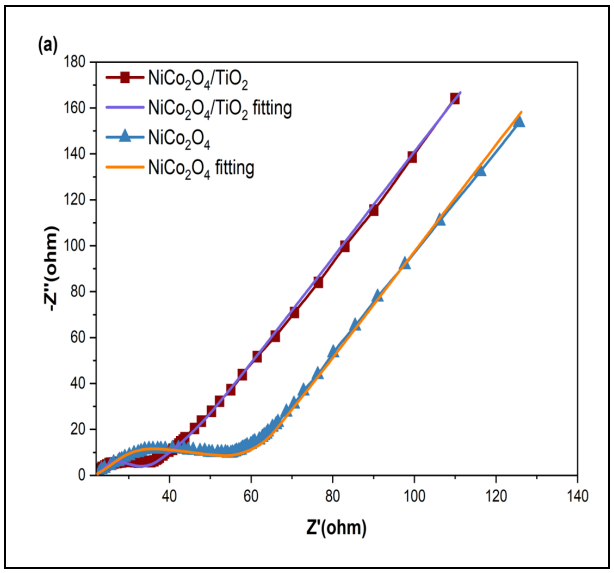


Fig. 16: Nyquist plots with fitted impedance of $NiCo_2O_4$-based electrodes

Table 1. Summary of resistance parameters and their EC-lab fitting deviations

Electrode	R_{ct} (Ω)	R_s (Ω)	Deviation
$NiCo_2O_4$–TiO_2	20	23.2	3.0
$NiCo_2O_4$ NPs	35	22.5	NA
$NiCo_2O_4$@N-C	300	22.5	2.5

The electrochemical impedance spectra were analyzed using an equivalent circuit model consisting of solution resistance (R_s), charge-transfer resistance (R_{ct}), and Warburg diffusion impedance (Z_w), which adequately fits the experimental Nyquist plots. The significantly reduced R_{ct} value (~20 Ω) for the $NiCo_2O_4$@N-C/TiO_2 nanocomposite indicates faster interfacial charge-transfer kinetics, resulting from the synergistic effect of nitrogen-doped carbon coating and the conductive TiO_2 matrix. The nearly unchanged R_s values among the electrodes suggest similar electrolyte resistance, while the reduced Warburg impedance for the nanocomposite reflects enhanced ion diffusion within the porous electrode structure. These fitting parameters collectively confirm improved electrical conductivity, accelerated redox reactions, and superior electrochemical performance of the $NiCo_2O_4$@N-C/TiO_2 electrode.

Table 2. Performance comparison of $NiCo_2O_4$@N-C/TiO_2 with other $NiCo_2O_4$-based supercapacitor electrodes in recent studies

S. No.	Material	Key Performance	Cycling Stability	Reference
1	$NiCo_2O_4$/$NiCoSnS_4$ oxide–sulfide hybrid	1120 F g^{-1} at 1 A g^{-1}	88% after 5000 cycles	(Verma *et al.* 2025)
2	Oxygen-vacancy-rich $NiCo_2O_4$ nanosheets	1812 F g^{-1} at 1 A g^{-1}	91.5% at 20 A g^{-1}	(You *et al.* 2023)
3	$NiCo_2O_4$@TiO_2 micro-heterojunction	735 F g^{-1} at 1 A g^{-1}	83% after 4000 cycles	(Xue *et al.* 2 019)
4	$NiCo_2O_4$/activated carbon composite	612 F g^{-1} at 1 A g^{-1}	85% after 3000 cycles	(Bosco Franklin *et al.* 2024)
5	$NiCo_2O_4$ nanoflowers (defect-engineered)	Energy density 42 Wh kg^{-1}	~90% retention	(Kannangara *et al.* 2024)
6	Carbon-modified $NiCo_2O_4$ on Ni foam	379.4 mF cm^{-2}	87.1% retention	Yang *et al.* 2024
7	$NiCo_2O_4$@N-C/TiO_2	709 F g^{-1} at 1 A g^{-1}	~80% after 10^3 cycles	Present work

Elevated solution resistance of $NiCo_2O_4$@N-C nanoparticles and the $NiCo_2O_4$@N-C/TiO_2 nanocomposite compared to the pristine $NiCo_2O_4$ nanoparticles can be attributed to the existence of the carbon covering. Reduced diameter of the semicircle for $NiCo_2O_4$@N-C nanoparticles, even more prominently for $NiCo_2O_4$@N-C/TiO_2, indicates lower charge transfer resistance (R_{ct}). A reduced R_{ct} rate signifies an efficient charge transfer procedure within the nanocomposite. The steep slope of the impedance curve in the low-frequency region for the $NiCo_2O_4$@N-C/TiO_2 nanocomposite indicates dominant capacitive behavior. The Warburg impedance is associated with the diffusion of electrolyte ions within the porous electrode. A Warburg impedance indicates shorter ion diffusion pathways within the electrode structure. Additionally, a capacitance (F g^{-1}) vs. frequency (kHz) plot was constructed to evaluate the ion transport kinetics. The Nyquist plot of the pristine $NiCo_2O_4$ electrode and the capacitance vs. frequency plot of the specimens are shown in Fig. 17.

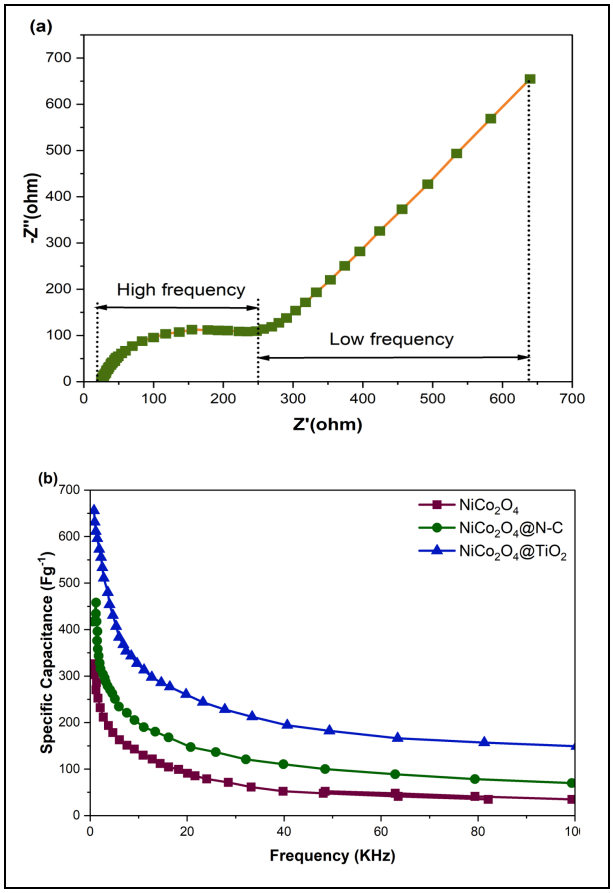


Fig. 17: (a) Nyquist plot of pristine $NiCo_2O_4$ electrode in 4 M KOH and (b) capacitance vs. frequency plot of the specimens

Table 2 compares the electrochemical performance of the present $NiCo_2O_4$@N-C/TiO_2 electrode with recent $NiCo_2O_4$-based materials. It demonstrates that the proposed nanocomposite exhibits competitive capacitance and charge-transfer characteristics, despite the conservative cycling evaluation.

4. CONCLUSION

This study reports the successful synthesis of nitrogen-doped carbon–coated $NiCo_2O_4$ nanoparticles and their TiO_2-integrated nanocomposite for supercapacitor applications. Structural and morphological analyses confirmed the formation of a stable spinel phase, with reduced agglomeration and improved surface accessibility due to carbon coating and TiO_2 incorporation. The $NiCo_2O_4$@N-C/TiO_2 electrode exhibited enhanced electrochemical performance, delivering a high gravimetric capacitance of 709 F g^{-1} at

1 A g^{-1}, reduced charge-transfer resistance (~20 Ω), and approximately 80% capacitance retention after 10^3 charge–discharge cycles. Although extended cycling beyond 10^4 cycles is required for full device-level validation, the present results demonstrate reliable short-term stability and effective pseudocapacitive behavior. Compared with previously reported $NiCo_2O_4$-based electrodes, the proposed nanocomposite exhibits competitive capacitance and improved charge-transfer characteristics, highlighting its potential for application in hybrid supercapacitors. Further optimization and full-cell assembly are expected to establish its practical applicability in next-generation energy storage systems.

FUNDING

This research received no specific grant from any funding agency in the public, commercial, or not-for-profit sectors.

CONFLICTS OF INTEREST

The authors declare that there is no conflict of interest.

COPYRIGHT

This article is an open-access article distributed under the terms and conditions of the Creative Commons Attribution (CC BY) license (http://creativecommons.org/licenses/by/4.0/).



REFERENCES

Bosco Franklin, J., Priyadharshini, V., Sundaram, S. J., Muthupandi, S. and Raj, D. A., Intrinsic pseudocapacitive enhancement of $NiCo_2O_4$/activated carbon composites, *Inorg. Chem. Commun*., 163, 112402 (2024). https://doi.org/10.1016/j.inoche.2024.112402

Edlabadkar, A. P., Mudadla, B., Karthick, K., Kumar, M. S., Adams, A. and Selvaraju, M., Optimization of machining parameters of AA2024/ZrO_2 MMC using TOPSIS, *J. Environ. Nanotechnol.,* 14(1), 181–192 (2025). https://doi.org/10.13074/jent.2025.03.2441016

Jiang, J., Leng, X., Zhang, Z., Chen, X., Hu, K. and Han, S., Sulfur-anchored oxygen vacancies boost ion storage in supercapacitor electrodes, *Energy*, 339, 138957 (2025). https://doi.org/10.1016/j.energy.2025.138957

Kannangara, Y. Y., Shadeepa, K., Wijesinghe, W. P. S. L., Chanaka, S., Ratwani, C. R., Kamali, C. R., Ali, R. K. and Amir, A. M., Electrochemical performance of $NiCo_2O_4$ nanostructures in hybrid supercapacitors: role of crystalline defects, *J. Energy Storage*, 84, 110717 (2024). https://doi.org/10.1016/j.est.2024.110717

Khawale, V. R., Mayank, Kumar, R., Satishkumar, P., Barun, H., Deepa, B., Rajasekaran, S., Veeramanikandan, P., Babu, P. A. S. and Mayakannan, S., Electrochemical stability and charge transfer efficiency of Fe_2O_3 nanorods for supercapacitors, *J. New Mater. Electrochem. Syst*., 27(3), 163–171 (2024). https://doi.org/10.14447/jnmes.v27i3.a01

Kizhepat, S., Rasal, A. S., Demissie, G. G., Gurav, V., Ghule, A. V. and Chang, J. Y., Impact of Mott–Schottky n–n junction in $NiCo_2O_4$/$Co(OH)_2FeOOH$ heterostructure for enhanced supercapacitor performance, *J. Power Sources*, 649, 237435 (2025). https://doi.org/10.1016/j.jpowsour.2025.237435

Ni, X., Li, K., Li, C., Wu, Q., Liu, C., Chen, H., Wu, Q. and Ju, A., $NiCo_2O_4$ nanoflake arrays on cellulose-derived carbon nanofibers as freestanding electrodes, *Front. Chem. Sci. Eng*., 17(6), 691–703 (2023). https://doi.org/10.1007/s11705-022-2268-6

Peng, M., Tian, X., Li, D., Wang, Q. and Zhang, D., Flexible asymmetric supercapacitors based on PANI@CNT–graphene and $NiCo_2O_4$@N–C electrodes, *Mater. Lett*., 272, 127859 (2020). https://doi.org/10.1016/j.matlet.2020.127859

Ran, J., Liu, Y., Feng, H., Zhan, H. and Yang, S., Green hydrothermal synthesis of $NiCo_2O_4$@MoS_2/RGO ternary composites for electrode applications, *J. Ind. Eng. Chem.,* 133, 273–283 (2024). https://doi.org/10.1016/j.jiec.2023.11.065

Sasmal, A., Nayak, A. K., Khan, M. E., Ali, W., Ali, S. K. and Bashiri, A. H., N and Mn doped $NiCo_2O_4$ functional nanostructures for symmetric supercapacitors, *Phys. Scr.,* 99(8), (2024). https://doi.org/10.1088/1402-4896/ad5c15

Satishkumar, P., Gopal, G., Meenakshi, R. and Vijayan, S. N., Tribological characteristics of powder metallurgy processed Cu–WC/SiC metal matrix composites, *Mater. Today Proc*., 37, 459–465 (2020). https://doi.org/10.1016/j.matpr.2020.05.449

Selvaraju, M., Rathinam, R., Rajasekaran, S., Deepalakshmi, R., Gopal, M., Maria, H. J. J., Nanthakumar, S., Ganvir, V. Y. and Singh, P., Spectroscopic and morphological analysis of surface-modified TiB_2 nanoparticles, *J. Nanomater.,* 2022(1), 1033216 (2022). https://doi.org/10.1155/2022/1033216

Shen, B., Liao, X., Hu, X., Ren, H. T., Lin, J. H., Lou, C. W. and Li, T. T., Hollow nanoflower $NiCo_2O_4$@Nb_2CT_x MXene heterostructure for flexible supercapacitors, *J. Mater. Chem. A*, 11(31), 16823–16837 (2023). https://doi.org/10.1039/d3ta02729e

Sun, X. and Jian, Z., Core–shell Co_3O_4@$NiCo_2O_4$ electrodes grown on Ni foam for high-performance supercapacitors, *J. Solid State Electrochem*., 28(8), 2659–2667 (2024). https://doi.org/10.1007/s10008-024-05808-7

Syed, O. B., Nithiyapathi, C., Rathinam, R., Nanthakumar, S., Gangwar, P. K. and Satishkumar, P., Mechanical and thermal properties of polypropylene composites reinforced with banana and sisal fibres, *Mater. Sci. Forum*, 1136, 15–28 (2024). https://doi.org/10.4028/p-dcWLj8

Verma, A., Tripathi, M. M., Mordina, B., Mukhopadhyay, K., Dwivedi, M. and Banerjee, S., Oxide–sulfide integrated $NiCo_2O_4$/$NiCoSnS_4$ composites for supercapacitors, *J. Energy Storage*, 140, 119090 (2025). https://doi.org/10.1016/j.est.2025.119090

Wu, J., Zhao, H., Li, L., Shen, H., Xu, J., Liang, X., Lan, Z. Zhou, W., Guo, J. and Huang, H., Enhanced electrochemical storage capability of $NiCo_2O_4$ nanosheet/nanowire hybrid arrays via synergistic MXene/graphene collaboration, J. Power Sources, 642, 236936 (2025). https://doi.org/10.1016/j.jpowsour.2025.236936

Xue, C., Chen, Y., Li, Y., Chen, H., Cui, D. and Lin, L., $NiCo_2O_4$@TiO_2 micro-heterojunction electrodes for supercapacitors, Appl. Surf. Sci., 493, 994–1003 (2019). https://doi.org/10.1016/j.apsusc.2019.06.285

Yang, X., Jin, X., Feng, H., Tian, L., Liu, L., Ding, J., Qamar, N. and Xing, Z., Carbon-modified $NiCo_2O_4$ as electrode material for supercapacitors, *J. Phys. Chem. Solids,* 193, 112208 (2024). https://doi.org/10.1016/j.jpcs.2024.112208

You, W., Li, M., Li, Q., Jiang, J., Xiang, K. and Xie, M., Oxygen defect-mediated $NiCo_2O_4$ nanosheets for pseudocapacitors, *Phys. Chem. Chem. Phys*., 25(36), 24862–24870 (2023). https://doi.org/10.1039/d3cp01924a

Yuan, B., Su, Z., Chen, K., Wang, J., Chen, B., Jiang, S., Yan, J., Chen, Z., Xie, A. and Luo, S., In-situ grown $NiCo_2O_4$ nanoparticles on lignin-derived porous carbon/MWCNT composites, *Diam. Relat. Mater*., 136, 110079 (2023). https://doi.org/10.1016/j.diamond.2023.110079

Zhang, J., Wu, T., Gu, Y. -J., Wen, W., Ye, Z. and Wu, J.-M., NiFeMn-LDH coated $NiCo_2O_4$ nanowires for ultra-long-life supercapacitors, *J. Power Sources*, 658, 238292 (2025). https://doi.org/10.1016/j.jpowsour.2025.238292

Zhang, Y., Chen, J., Ma, Y., Yang, X. and Li, Y., Enhanced energy storage in dandelion-like $NiCo_2O_4$/$Ti_3C_2T_x$ MXene composite via heterointerface design for supercapacitor, *J. Alloys Compd.,* 1044, 184623 (2025). https://doi.org/10.1016/j.jallcom.2025.184623

Zhu, X., Zhu, P., Li, Y. and Liu, Y., Nickel cobalt oxide nanowires with oxygen vacancies on CVD graphene networks for asymmetric supercapacitors, *J. Energy Storage,* 104, 114546 (2024). https://doi.org/10.1016/j.est.2024.114546